SEMARAK ILMU PUBLISHING

Journal of Advanced Research in Fluid Mechanics and Thermal Sciences

Journal homepage:
https://semarakilmu.com.my/journals/index.php/fluid_mechanics_thermal_sciences/index
ISSN: 2289-7879

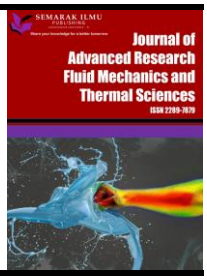

High-Fidelity Conjugate Heat Transfer Simulation of Micro-Channel Heat Exchanger

Hossain Ahmed[1], Hamid Sadat[1,*], Seifollah Nasrazadani[1]

[1] Department of Mechanical Engineering, University of North Texas, Denton, Texas 76207, United States

ARTICLE INFO

Article history:
Received 27 January 2023
Received in revised form 5 May 2023
Accepted 11 May 2023
Available online 24 May 2023

Keywords:
Computational Fluid Dynamic (CFD); Microchannel Heat Exchanger (MCHE); conjugate heat transfer

ABSTRACT

In this study, high-fidelity conjugate heat transfer simulations are used to model a micro-channel heat exchanger (MCHE) in a crossflow to study its thermal-hydraulic performance. Three different microchannel geometries, namely circular, triangular, and square with louver-shaped fins, are considered. The local flow field showed a strong coupling between the microchannel flow, solid domain, and crossflow. The flow separation and wake regions formed near MCHE resulted in a large variation in the velocity field and temperature in the crossflow. The interaction of the wake region with the fins introduces significant spanwise variations, leading to variations in the thermal boundary layer. The heat conduction in the solid structure provided a non-uniform temperature field with a higher temperature near the microchannel and a slightly lower temperature near the surface exposed to the crossflow. The microchannel flow analysis showed that the internal geometry affects the pressure drop, which is highest for the triangular MCHE and lowest for the circular MCHE. Based on the effectiveness and performance index calculations, the circular MCHE exhibited the best performance, while the rectangular MCHE showed higher heat transfer effectiveness.

1. Introduction

In recent years, there has been a significant increase in research focused on thermal-hydraulic phenomena at the microscale level. This is driven by the growing demand for efficient heat transfer in compact spaces and volumes, as required in various industries including automotive, aerospace, power generation, chemical processing, gas delivery systems, and fuel cell technologies [1-11].

Numerous studies have been conducted to investigate the performance of microchannel heat exchangers (MCHEs) over the past two decades. Dang *et al.,* [12] conducted both experimental and computational fluid dynamics (CFD) simulations, identifying key parameters influencing MCHE performance, such as pressure drop, inlet flow velocity, microchannel roughness or cavity, and channel sizes and shapes. Herman *et al.,* [13] observed that increasing fluid velocity improves heat transfer performance but simultaneously increases pressure drop. Pan *et al.,* [14] reported that MCHEs with fan-shaped cavities exhibit enhanced heat transfer performance and lower pressure

* *Corresponding author.*
E-mail address: hamid.sadat@unt.edu

https://doi.org/10.37934/arfmts.106.1.165181

drop compared to straight channels. Jiang *et al.,* [15] conducted experimental investigations on rectangular MCHEs with different channel heights, finding that MCHEs with deeper channels have lower pressure drop for the same flow rate and superior overall thermal-hydraulic performance. Brandner *et al.,* [16] studied various microstructure crossflow heat exchangers and compared their thermal performance. They discovered that reducing the hydraulic diameter of microchannels improves heat transfer in micro heat exchangers. Additionally, they fabricated heat exchangers with two different layouts of microcolumn arrays (aligned and staggered), demonstrating that the array configuration maximizes heat transfer while minimizing pressure drop across the heat exchanger.

To investigate the MCHE performance, several researchers have employed CFD with various levels of fidelity. Hasan *et al.,* [17] conducted a numerical investigation of laminar, three-dimensional fully developed flow in MCHEs with circular, triangular, square, and trapezoidal microchannel shapes. Their results indicated that the circular microchannel shape exhibited the best overall thermal-hydraulic performance, while the square microchannel shape ranked second. However, regardless of the microchannel shape, the performance decreased with increasing Reynolds number. Sui *et al.,* [18] conducted a numerical study on laminar water flow and heat transfer in three-dimensional wavy microchannels with a rectangular cross-section. They found that, for microchannels with the same cross-sectional area, the wavy configuration exhibited better heat transfer performance compared to straight microchannels, albeit with a relatively smaller pressure drop. Al-bakhit *et al.,* [19] investigated the performance of MCHEs with parallel flow and rectangular ducts. They observed that the overall heat transfer coefficient experienced a significant change in the entrance region of the duct, where the Graetz number was less than 0.03. This finding indicated that the assumption of a constant overall heat transfer coefficient is not always valid for the entrance region.

One of the limitations observed in the previously mentioned numerical analyses is the absence of crossflow modelling, where the effect of crossflow was often assumed by imposing constant temperature or constant heat flux on the surfaces of the MCHE. To the best of our knowledge, only two studies conducted by Glazar *et al.,* [20] and Ahmed *et al.,* [21] accounted for crossflow by incorporating it into their CFD models. Glazar *et al.,* [20] primarily focused on MCHE optimization with oversimplified fin shapes. Ahmed *et al.,* [21] demonstrated the significance of crossflow modeling in understanding the corrosion pattern on MCHE surfaces. In this study, high-fidelity conjugate heat transfer simulations are employed to investigate the thermal-hydraulic performance of an MCHE featuring louver-shaped fins in the presence of crossflow. The solid domain, microchannel flow, and crossflow field are tightly coupled to accurately predict the temperature of the solid and flow field variables and temperature in both microchannel and crossflow regions. This study considers three MHCEs with different microchannel geometries (circular, triangular, and square).

2. Methodology

2.1 Geometry

In order to minimize computational costs, the CFD computational model focuses on a small section of an MCHE tube, featuring five louver-shaped fins attached to it, as illustrated in Figure 1. Due to the symmetric conditions of the MCHE, only half of the fin's height on each side of the tube is considered. The dimensions of the selected section of the MCHE are l×w×h=0.4×0.07×0.05 cubic inches. Three different microchannel geometries, namely circular, triangular, and rectangular, are examined for the tube. Despite having the same volume (4.882×10^{-5} inch^3), these microchannels possess different hydraulic diameters, as indicated in Table 1. The simulation adopts a coordinate system where the Z-axis aligns with the microchannel axis. The Y-axis runs parallel to the fin surfaces and along the height of the flat tube, while the X-axis aligns with the width of the flat tube.

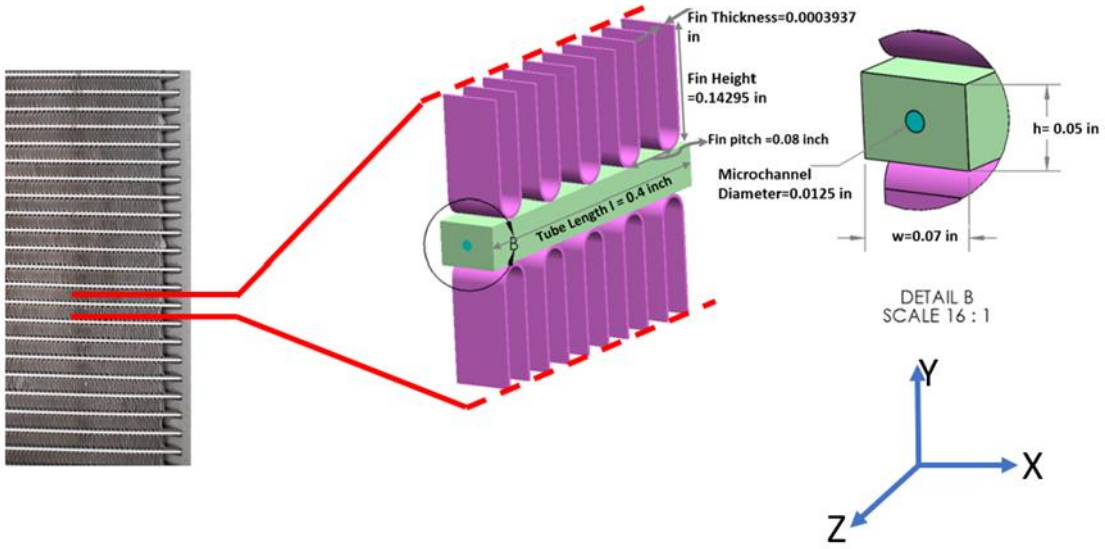

Fig. 1. Schematic diagram of a characteristic part of MCHX

Table 1
Geometry specification of MCHE

Microchannel Shape	Circular
Parameter	Value
Tube length l (inch)	0.4
Tube height h (inch)	0.05
Tube Width w (inch)	0.07
Hydraulic Diameter (inch)	0.0125 (Circular) 0.00972 (Triangular) 0.01108 (Rectangular)
Microchannel volume (inch^3)	4.8819×10^{-5}
Fin type	Louver
Fin thickness (inch)	0.0003937
Fin height (inch)	0.14295
Fin pitch (inch)	0.08

2.2 CFD Method

The segmental MCHE was simulated using ANSYS Fluent. Governing equations for the mass, momentum, and energy are solved using the finite volume method and non-staggered grid discretization for incompressible flow.

$$\nabla . \vec{v} = 0 \tag{1}$$

$$\rho \frac{\partial}{\delta t}(\vec{v}) + \nabla . (\rho \vec{v} \vec{v}) = -\nabla \mathrm{p} + \mu \nabla^2 \vec{v} + F \tag{2}$$

$$\rho C_p \frac{\partial T}{\partial t} + \rho C_p \vec{v} . \nabla \mathrm{T} = \nabla . (\mathrm{k} \nabla \mathrm{T}) + \emptyset \tag{3}$$

where the static pressure p, molecular viscosity μ, velocity field $\vec{v}$, temperature T, specific heat at constant pressure C_p, body force F and dissipation function $\emptyset$ represents the work done against viscous forces.

For the solid side, the following heat conduction equation is solved

$$\rho C_p \frac{\partial T}{\partial t} = \nabla.(\mathrm{k}\nabla T) + \emptyset \tag{4}$$

The governing equations and boundary conditions have been discretized using the finite volume method. The fluids are assumed to be incompressible, with constant physical properties, and the flows are considered to be laminar and steady. As a result, the temporal terms in the equations are neglected. To handle the pressure-velocity coupling, a coupled algorithm is utilized, which solves the momentum and continuity equations simultaneously, in contrast to predictor-corrector segregated methods. The convection-diffusion terms are discretized using the second-order Upwind scheme.

2.3 Computational Domain, Boundary Conditions, and Grids

The computational domain consists of three main regions: the crossflow, microchannel flow, and solid regions. Figure 2 provides a schematic view of the computational domain. The crossflow domain is divided into three sections: the inlet region, the region between the fins, and the outlet region. The crossflow domain extends from X~-7w (0.5 inch) to X~18w (1.25 inch), where w represents the width of the tube. The width and height of the crossflow domain match the width and height of the simulated section of the MCHE. The microchannel flow domain has a length of L=0.4 inch. For the cylindrical microchannel geometry, the diameter is 0.0125 inch, while for the triangular and square microchannels, the hydraulic diameters are 0.00972 inch and 0.01108 inch, respectively. The solid domain consists of two regions: the tube and the louver-shaped fin.

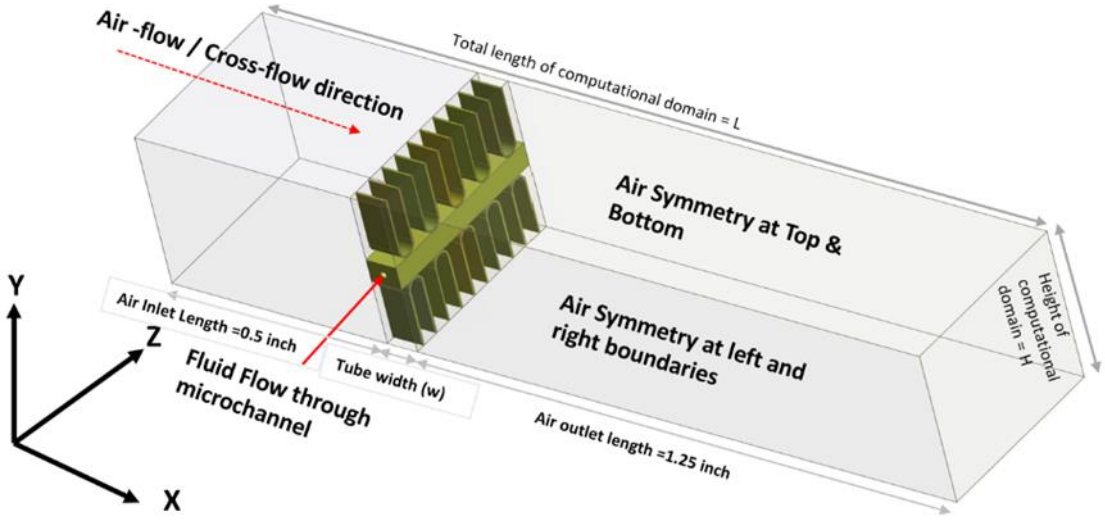

Fig. 2. Computational domain for MCHE with Step shape fin

In the crossflow domain, unstructured quadrilateral/hexahedral grids are used. The total number of grids in the crossflow domain is approximately 4.5 million, as specified in Table 2. On the other hand, for the solid domain encompassing the fins and tube, a structural hexahedral mesh is employed, as depicted in Figure 3. Each fin's inner and outer surface is represented by a surface grid with dimensions of 65 grids along the fin's width and 248 grids along its length. The surface grids are used to generate the structured hexahedral grids for fins. The fins comprise a total of 0.8 million grids. Additionally, the tube consists of 3.3 million structured hexahedral grids. Regarding the microchannel, prism and hexahedral grids are employed. The streamwise direction of the

microchannel comprises 216, 205, and 225 grids for the circular, triangular, and square geometries, respectively. The microchannels comprise a total of approximately 43,000 grids. For each case, the overall grid count amounts to approximately 8.6 million grids, which are distributed among 32 cores for parallel processing.

Table 2
Grid sizes

Domain	Grid
Crossflow domain	4463186
Microchannel	43992 (Circular)
	42877 (Triangular)
	44154 (Square)
Fin	823857
Rectangular tube	3339600
All Domains	8670635 (Circular)
	8669520 (Triangular)
	8670797 (Square)

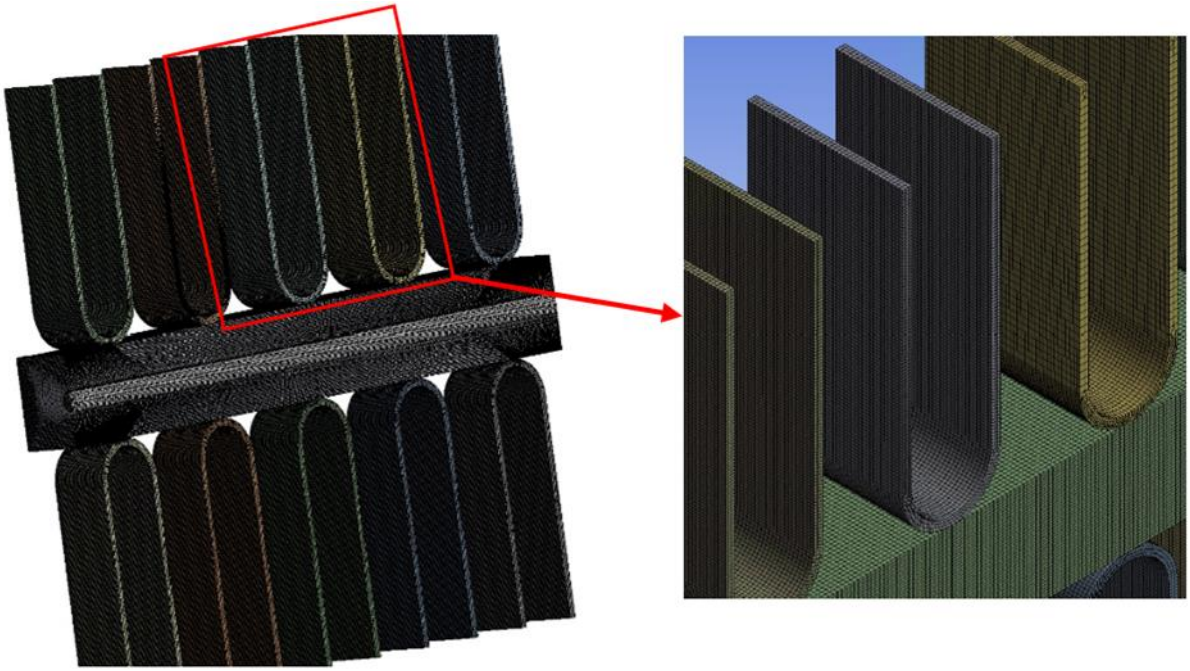

Fig. 3. Details of triangular prism and hexahedral mesh of circular MCHE with Step fin

In the crossflow domain, the inlet conditions are set to a velocity of 16 m/s and a temperature of 26.85 °C, as referenced in [22]. The outlet boundary is a pressure outlet, and the symmetric boundary condition is applied to all sides of the domain. The working fluid used in the crossflow domain is air, with properties such as a density (ρ_{air}) of 1.225 kg/m³ and a specific heat (C_p) of 1006.43 J/(kg·K). The Reynolds number (Re) on the airside, based on the width of the tube, is calculated to be 2×10^4, indicating that the fluid boundary layer on the surfaces of the MCHE can be assumed to be laminar. For the microchannel domain, the inlet velocity is set to 0.2 m/s, the exit boundary employs a zero velocity gradient condition, and a non-slip boundary condition is used at the wall. Water is used as the working fluid in the microchannel, with properties such as viscosity (μ) of 0.001003 kg/(m·s), specific heat (C_p) of 4182 J/(kg·K), and density (ρ) of 998.2 kg/m³. The Reynolds number on the microchannel side is calculated to be 149.73, indicating laminar flow. Since both the crossflow and

microchannel exhibit laminar flow in their respective Reynolds number range, the simulation employs the laminar model.

In the solid domain, the surfaces of the fins and the exterior surface of the tube are thermally coupled with the crossflow domain, while the interior surface of the tube is thermally coupled with the microchannel flow domain. The tube section has an inlet temperature of 26.85 °C. Symmetric boundary conditions are applied to the upper and lower boundaries of the fins, ensuring a zero temperature gradient $\frac{\partial T_{fin}}{\partial y} = 0$. Further details of the boundary conditions can be found in Table 3.

Table 3
Boundary conditions of the computational domains

Domains	Parts	Boundary conditions
Microchannel	Inlet (water inlet, z-direction)	$Velocity\ inlet;\ U_w = 0.2\ \frac{m}{s}$, Inlet temperature of the water, $T_{w,in} = 50℃$
	Outlet	Pressure outlet
	Wall	Via system coupling with solid for temperature; No-slip boundary condition for velocity
Solid (aluminum)	Inlet	Inlet temperature, $T_s = 26.85$ ℃
	Outlet	Heat flux=0
	Wall	Via system coupling with air for temperature; No-slip boundary condition for velocity
Fin (aluminum)	Top fin and bottom fin boundaries	Symmetric
Crossflow	Inlet (air inlet, x-direction)	$Velocity\ inlet;\ U_a = 16\ \frac{m}{s}$ (Inlet temperature of the air, $T_a = 26.85℃$
	Outlet	Pressure outlet
	Side boundaries	Symmetric

2.4 Grid Verification and Validation Study

A grid verification study was carried out by coarsening and refining the medium grid described earlier which resulted in grid sizes of 4.3 million cells for the coarse grid and 17.4 million cells for the fine grid. The results of the study demonstrated that the predicted centerline velocity in the microchannel undergoes a minor change of 0.27% from the coarse grid to the medium grid and a further 0.25% from the medium grid to the fine grid. These findings suggest that the results are relatively insensitive to variations in the grid size.

Figure 4 also presents the comparison between the analytical velocity profile and the predicted one to validate the results. The findings demonstrate a good agreement between the predicted profile and the theoretical expectations. The maximum error is observed for the velocity at the centerline, with a discrepancy of 3.25% for the coarse grid, which reduces to 2.56% and 1.93% for the medium and fine grids, respectively.

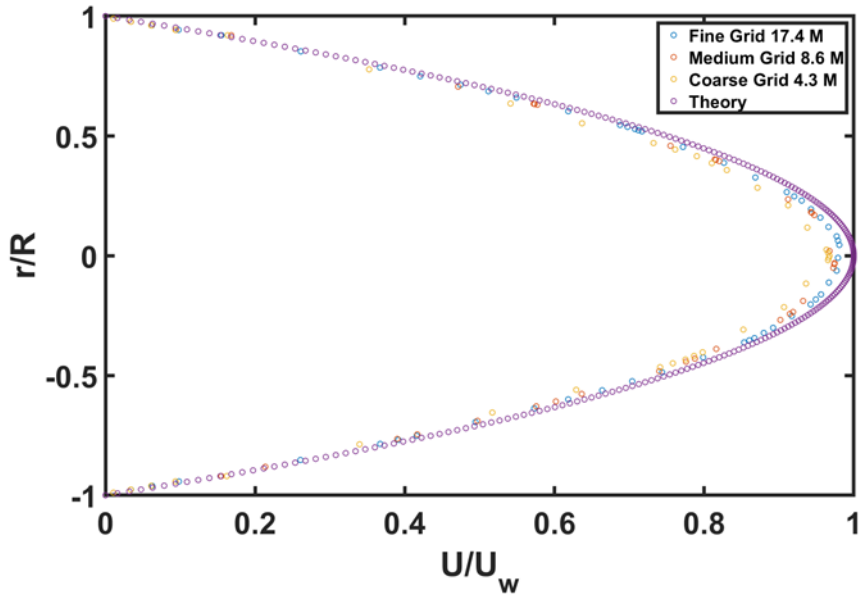

Fig. 4. Verification analysis for flow through circular microchannel

In Figure 5, the velocity profile in the crossflow domain is displayed for three distinct grid sizes along a line situated in both the streamwise and spanwise directions. Consistently, a comparable flow pattern is observed across all three grid sizes, signifying grid independence behavior within the crossflow domain.

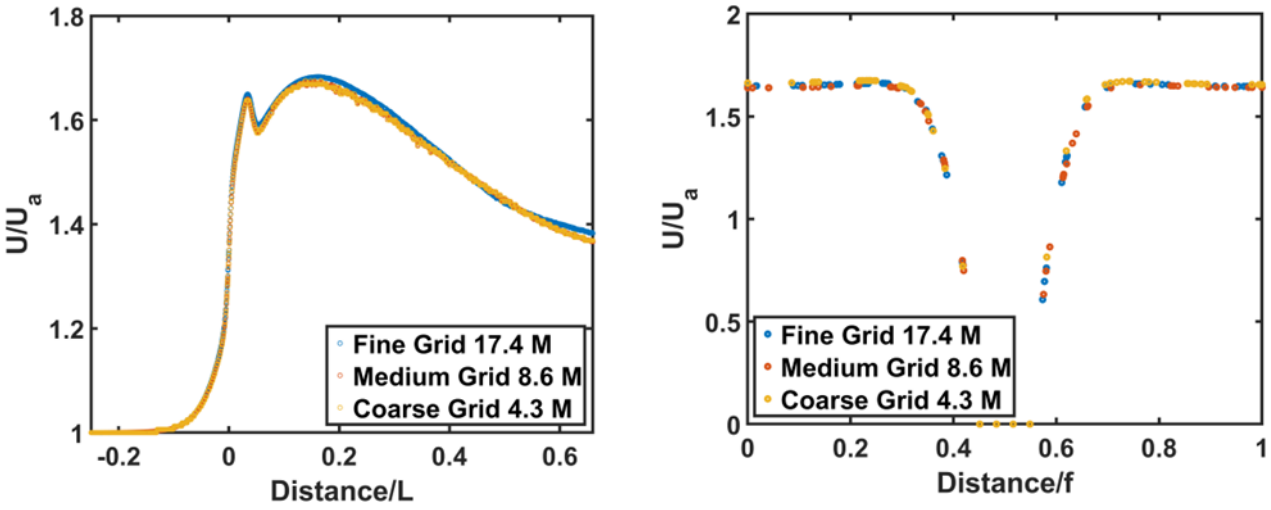

(a) (b)

Fig. 5. Verification analysis for airside a) streamwise direction b) spanwise direction

As the results remain insensitive to changes in the grid size, the medium grid is selected for all subsequent simulations.

3. Results

3.1 Crossflow Analysis

Figure 6 displays the velocity contour in the crossflow at various x locations, which are indicated in Figure 7. It should be noted that the MCHE is situated between x=0 and x=0.07 inches. As the flow progresses over the MCHE, a separated flow region develops on the tube's surface (as observed in

Figure 6 (a)-(c). The thickness of this separated region exhibits fluctuations in the spanwise direction, resulting in a larger separated region in region A, which is confined by each fin, compared to region B located in the gap between two consecutive fins. The spanwise variation of the wake field arises from the interaction of the fins with the flow field, leading to a lower velocity in region A compared to region B. Far from the solid surfaces, the velocity demonstrates an elevation relative to the inlet velocity. This increase in velocity occurs due to the combined effects of blockage and the formation of a boundary layer on the solid surfaces.

As the airflow progresses downstream of the MCHE, a substantial wake region becomes apparent, as depicted in Figures 6 (d)-(f). Within this expanded wake region, the presence of the Kelvin-Helmholtz instability at finite amplitude is observed.

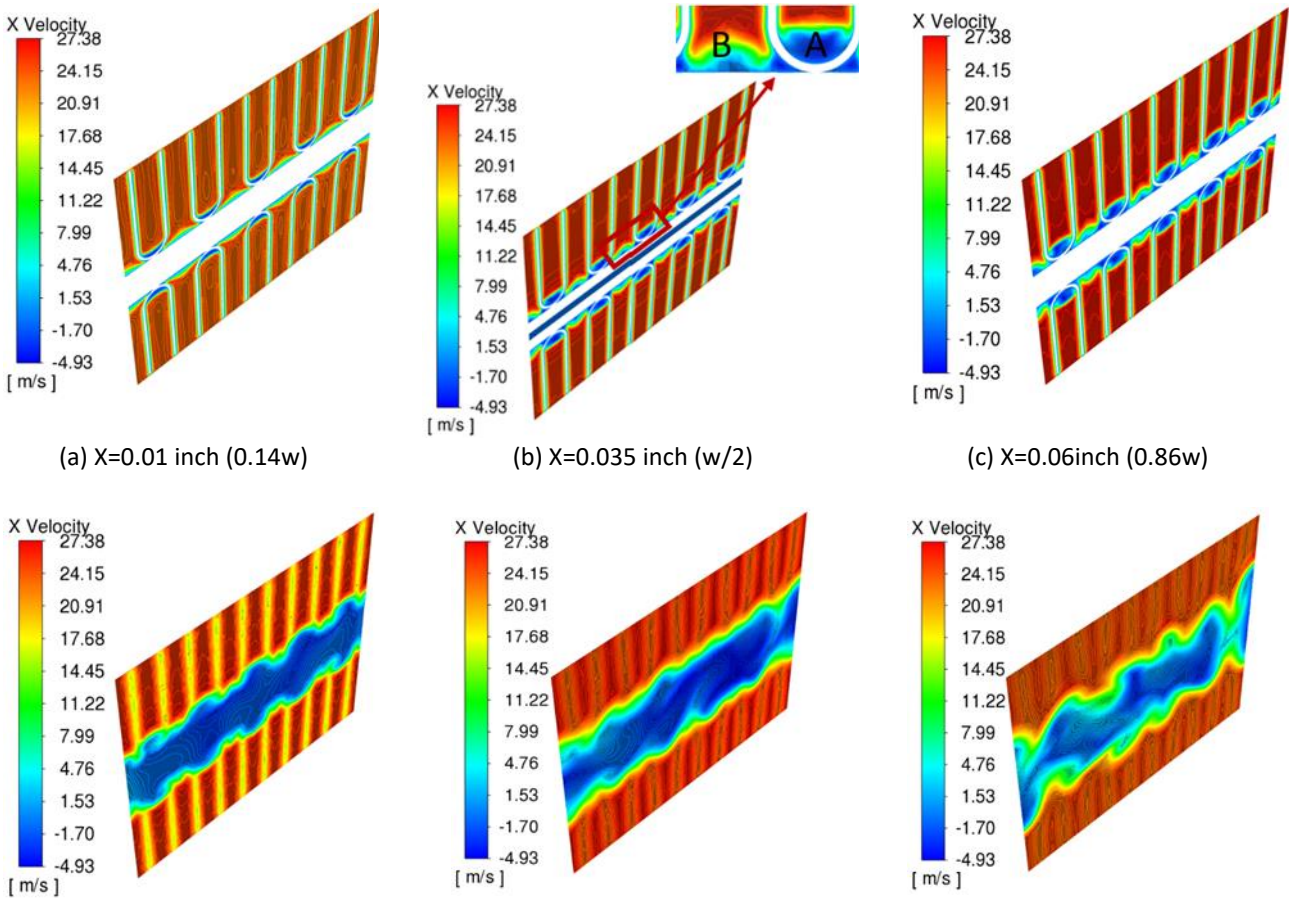

(a) X=0.01 inch (0.14w) (b) X=0.035 inch (w/2) (c) X=0.06inch (0.86w)

(d) X=0.1 inch (1.43w) (e) X=0.4 inch (5.7w) (f) X=0.7inch (10w)

Fig. 6. Velocity contour of crossflow for circular MCHE at different X location

Figure 7 exhibits the crossflow at the midplane. Prior to reaching the MCHE, the flow velocity appears uniform and comparable to the inlet velocity. However, as the flow interacts with the MCHE, flow separation transpires at the junction between the crossflow and the solid tube. This results in the solid tube being immersed within the separated flow region. Furthermore, the crossflow velocity intensifies around the MCHE due to two contributing factors: the blockage effect caused by the presence of the MCHE and the formation of the separated region in proximity to the MCHE. Notably, the crossflow velocity reaches its maximum value at x=2.5w, corresponding to the location where the wake thickness is the greatest.

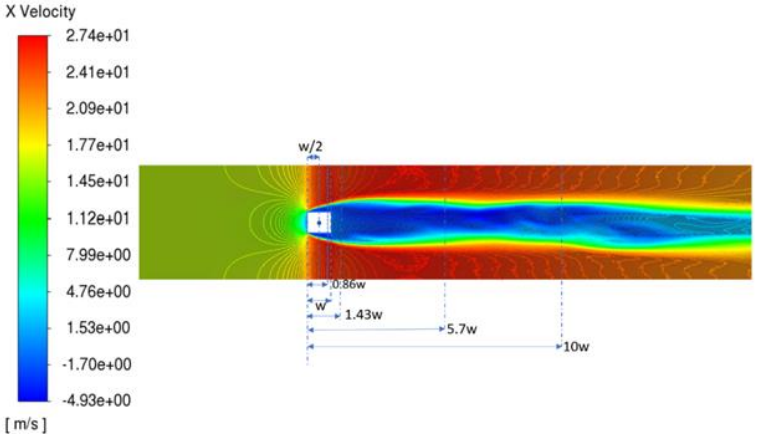

Fig. 7. Velocity contour of crossflow for circular MCHE at the center plane (z=0)

Figure 8 presents the temperature contour in the crossflow. In the vicinity of the MCHE (Figure 8(a)-(c)), the crossflow temperature exhibits an increase in proximity to the solid surface due to the presence of hot water flowing through the microchannel. As the flow progresses over the tube, the thermal boundary layer expands, coinciding with the increasing thickness of the separated region (as shown in Figure 7). The thickness of the thermal boundary layer fluctuates in the spanwise direction, mirroring the trends observed in the velocity field. Region A displays a larger thermal boundary layer thickness compared to region B. The temperature of the crossflow gradually decreases as the flow advances downstream, ultimately reaching the inlet air temperature, $T_a = 26.85$ °C.

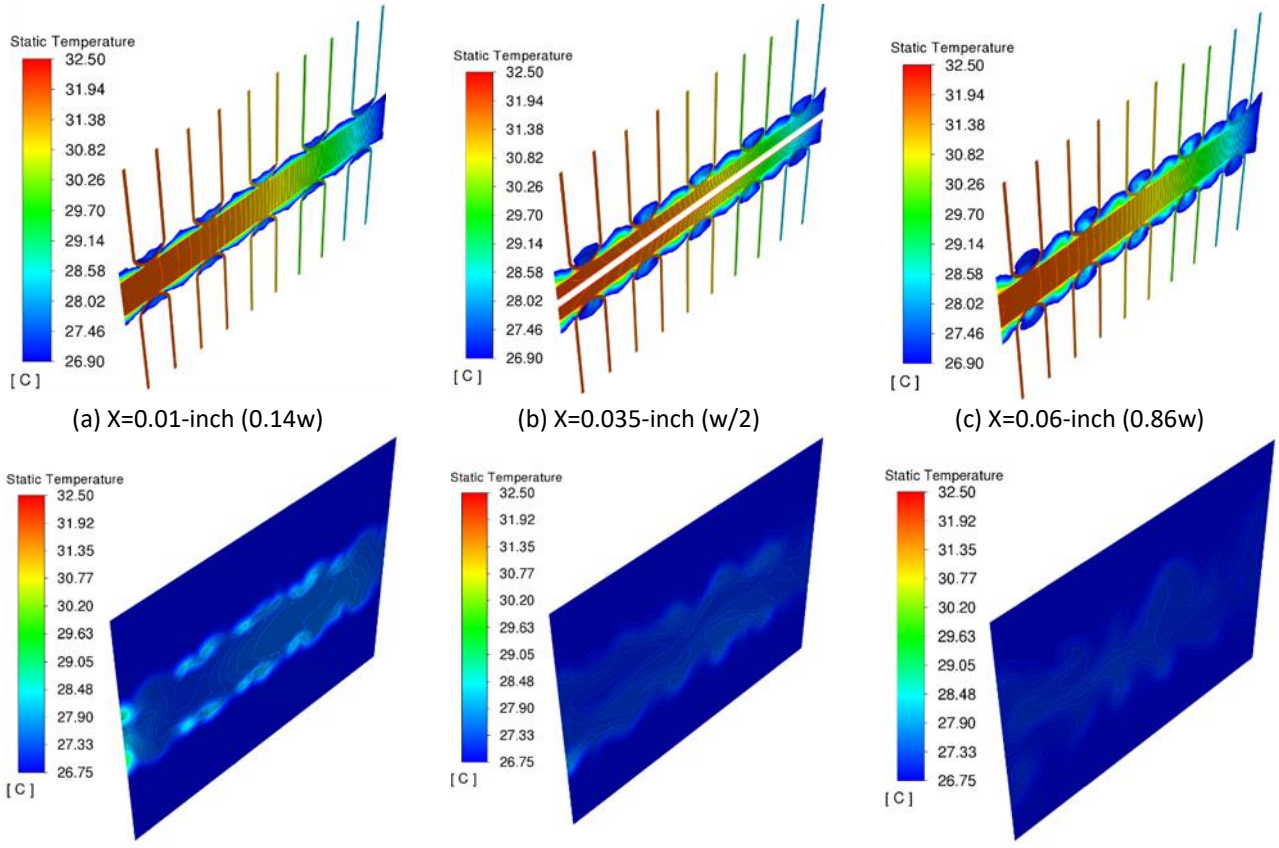

(a) X=0.01-inch (0.14w) (b) X=0.035-inch (w/2) (c) X=0.06-inch (0.86w)

(d) X=0.1-inch (1.43w) (e) X=0.4-inch (5.7w) (f) X=0.7-inch (10w)

Fig. 8. Temperature contour of crossflow for circular MCHE at different X location

Figure 9 showcases the streamwise velocity along four lines (P1 to P4) located at various y positions. The schematic diagram in Figure 9 provides specific details about the P locations, where P1 is positioned at a height of 0.18 inches, P2 at 0.12 inches, P3 at 0.08 inches, and P4 at 0.06 inches. In Figure 9(a), these lines are parallel to the x-axis, representing the crossflow direction. Figure 9(b) depicts the distribution of streamwise velocity along lines oriented in the z-axis direction, which corresponds to the spanwise direction.

In Figure 9(a), it is evident that the velocities along all the lines closely resemble the inlet velocity at the upstream region. As the flow progresses through the fins, the velocity increases to approximately 1.6 times the inlet velocity. Subsequently, the velocity experiences a significant drop for P3 and P4, and a slight reduction for P1 and P2, as the flow continues downstream. The substantial velocity decrease observed for P3, and P4 indicates that these lines are situated within the wake region downstream of the heat exchanger.

Figure 9(b) illustrates the streamwise velocity along the lines passing through P1-P4. At P1, the velocity is highest at points located away from the fin surface and gradually diminishes to zero at the fin surfaces. The velocity pattern exhibits symmetry with respect to the fin surface, indicating a similar velocity profile on both sides of the fin. A similar trend is observed along the line passing through P2. On the other hand, the velocity distribution along the line passing through P3 shows variations on different sides of the fin, with lower velocity observed where the boundary layer is thicker (as seen in region A in Figure 6). The velocity at P4 also displays an asymmetric profile, with lower velocity in the thicker boundary layer formed in region A.

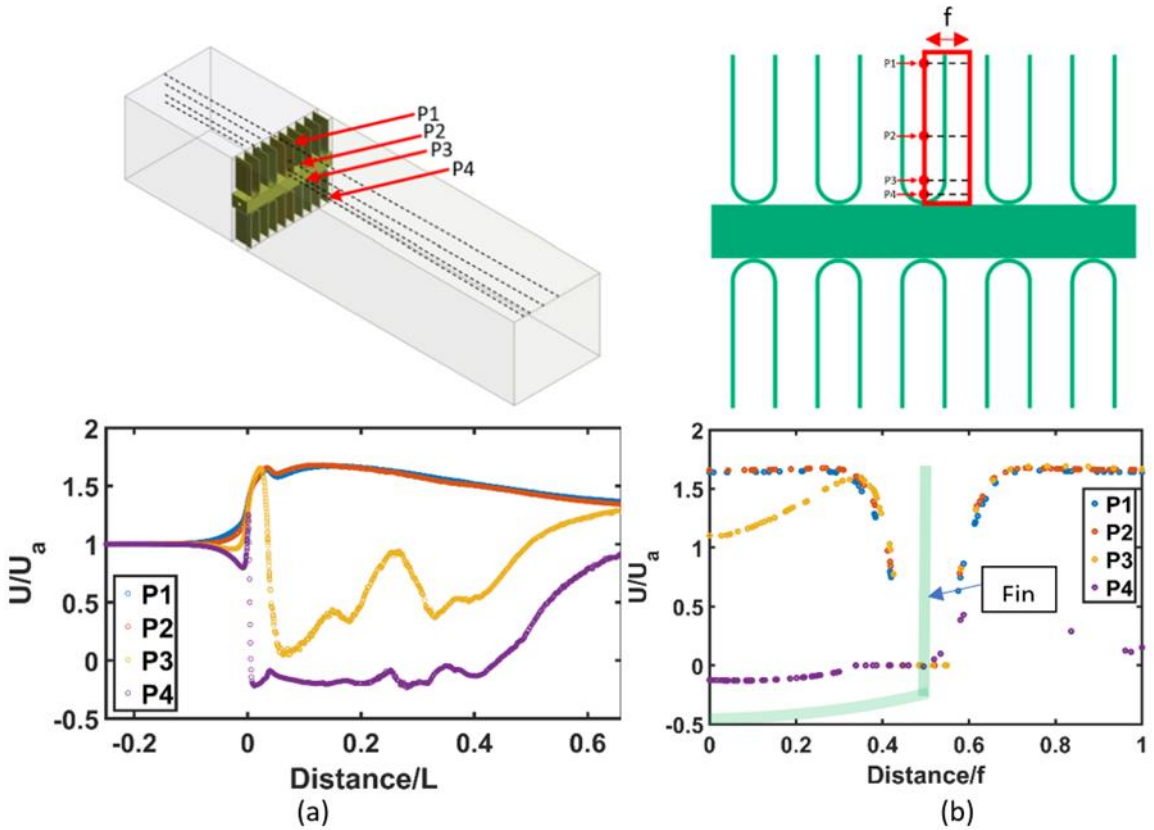

Fig. 9. Velocity flow distribution of crossflow for circular MCHE at P1, P2, P3, and P4 locations along (a) streamwise direction, and (b) spanwise direction

Figure 10 displays the temperature profiles along four lines (P1 to P4) situated at different y positions. In Figure 10(a), it is evident that the temperature along these lines initially closely

resembles the inlet temperature at the upstream region. As the flow traverses through the fins, the temperature undergoes an increase of approximately 7.8% at the location of P4 and 2.1% at the P3 position. However, the temperature remains relatively constant along the lines passing through points P1 and P2, as these points are located far away from the heat exchanger. Figure 10(b) shows that the temperature on the line passing through P4 exhibits the highest values since it is in closest proximity to the solid surface. Specifically, the temperature near the fin surface along line P4 is approximately 16% higher than the inlet temperature. As the line extends across the fin, the temperature drops asymmetrically on both sides, reaching values approximately 7-8% higher than the inlet temperature. When transitioning from P4 to the other lines, the crossflow temperature in close proximity to the fin surface remains relatively consistent for all lines (approximately 16% higher than the inlet temperature). However, as the distance from the fin surface increases, the temperature diminishes rapidly, reaching the inlet temperature along those lines due to their greater distance from the tube.

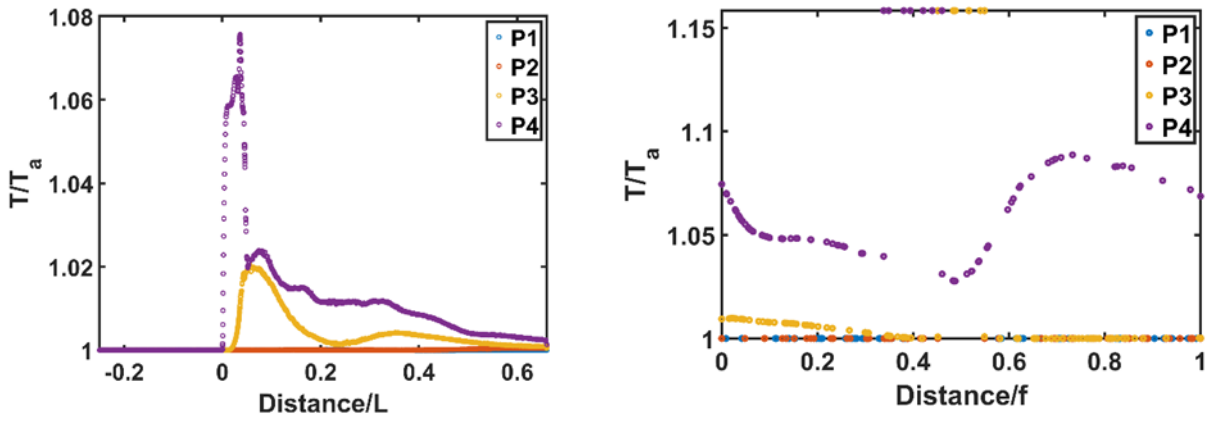

(a) (b)

Fig. 10. Temperature profile of crossflow for circular MCHE at P1, P2, P3 and P4 locations along (a) streamwise direction, (b) spanwise direction

Figure 11 displays the crossflow temperature distribution along lines near the solid surface (P3 and P4) for three different microchannel geometries, encompassing triangular, rectangular, and circular configurations. In Figure 11(a), it is apparent that the temperature values along all lines closely resemble the inlet temperature at the upstream region. At the P3 location, as the flow progresses within the fins, the temperature increases by approximately 3% for triangular microchannel heat exchangers, around 4% for rectangular microchannels, and approximately 2% for circular microchannels. Moving to the P4 position, as depicted in Figure 11(b), the temperature rises to approximately 15% higher than the inlet temperature for triangular microchannels, around 8% for circular microchannels, and roughly 6% for rectangular microchannels.

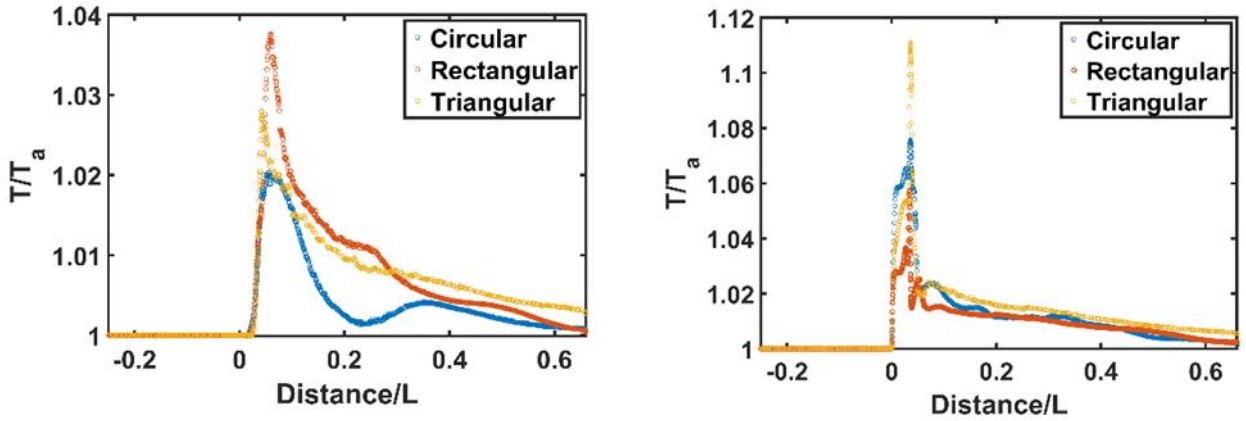

(a) P3 location (b) P4 location

Fig. 11. Temperature profile of crossflow along streamwise direction for different MCHE geometries at (a) P3 location, and (b) P4 location

Figure 12 showcases the temperature profiles at P3 and P4 along lines in the spanwise direction. The figures reveal that the temperature is highest in proximity to the fin surface, with values approximately 16% higher than the inlet temperature. At the P4 location, the temperature at points distant from the fin surface remains relatively consistent for all three microchannel geometries. Conversely, at the P3 location, slight variations in temperature are observed at points far from the fin surface among the different microchannel geometries.

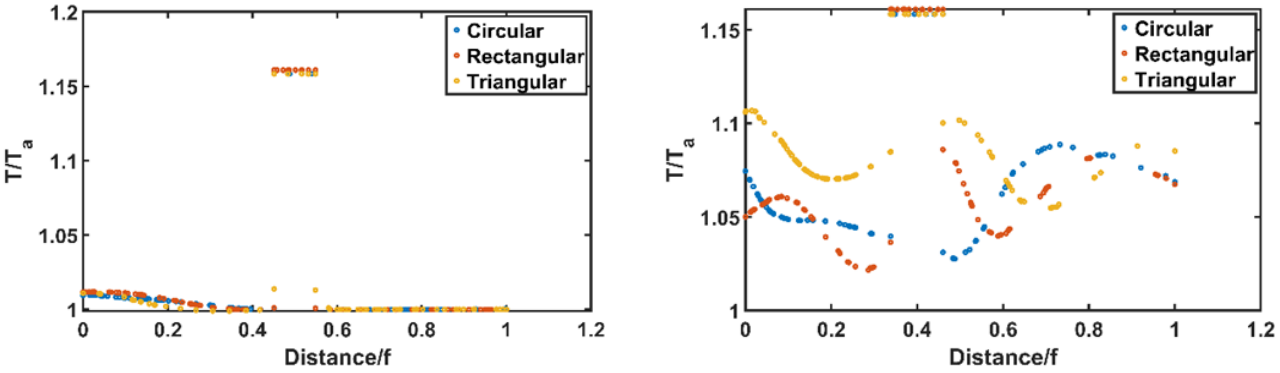

(a) P3 location (b) P4 location

Fig. 12 Temperature profile of crossflow along spanwise direction for different MCHE geometries at (a) P3 location, and (b) P4 location

3.2 Solid Domain Analysis

Figure 13 depicts the results obtained from two lines: one positioned on the backside surface of the tube and the other on the top surface of the tube. In Figure 13(a), the temperature profile along the backside line reveals that the temperature of the tube rises from its initial value as water flows through the microchannel. The increase in tube temperature is approximately 18% for all types of microchannel heat exchangers (MCHEs).

Figure 13(b) demonstrates that the temperature remains relatively uniform at the mid-section of the tube, with a slight variation among different MCHEs. The rectangular MCHE exhibits a slightly higher temperature, while the triangular MCHE shows a slightly lower temperature in this region.

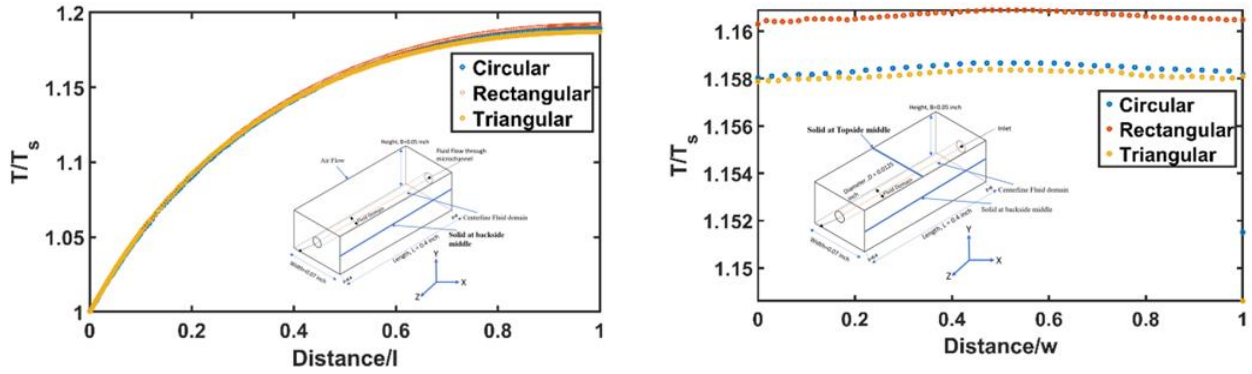

(a) (b)

Fig. 13. Temperature profile of tube at (a) backside middle, and (b) topside middle

Figure 14 and 15 depict the temperature distribution on the surfaces of the tube, fins, and microchannels for all the MCHEs considered in the study. The temperature of the tube and microchannel surfaces remains close to the inlet temperature of 26.8°C. As the solid domain of the MCHE is exposed to the hot flow within the microchannel, the temperature of these surfaces increases. The fins, made of highly conductive aluminum material, also exhibit the same temperature as the tube, indicating similar thermal performance across all the different MCHE geometries.

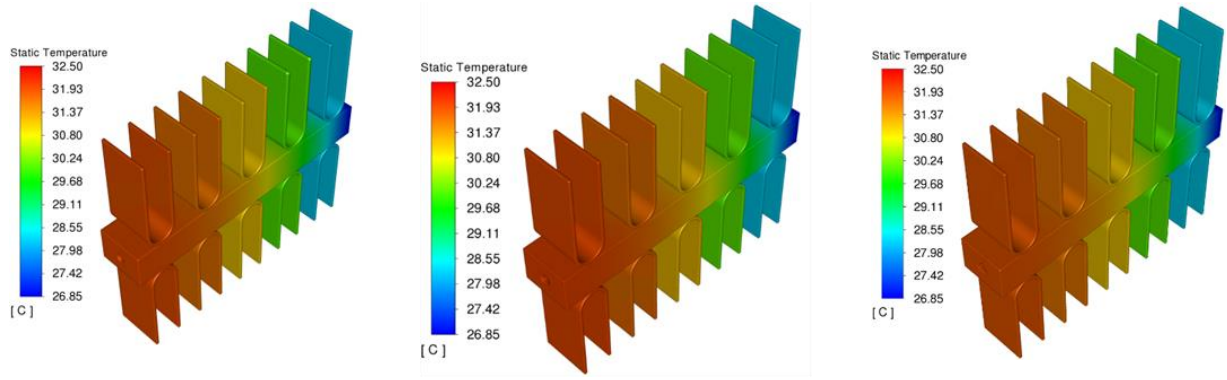

(a) Circular (b) Rectangular (c) Triangular

Fig. 14. Temperature contour on different MCHE

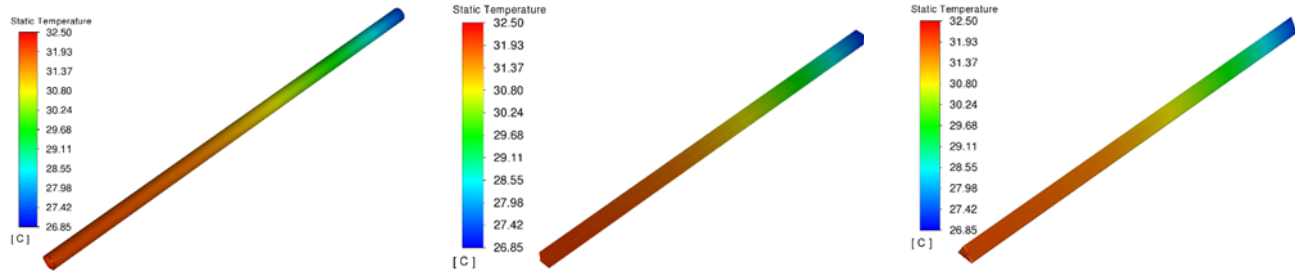

(a) Circular (b) Rectangular (c) Triangular

Fig. 15. Temperature contour on the surface of microchannel tube

3.3 Microchannel Analysis

Figure 16 presents the velocity, temperature, and pressure profiles along the centerline of the three microchannel geometries. In Figure 16(a), it can be observed that the centerline velocity of the circular microchannel increases and reaches a fully developed condition with a constant velocity approximately twice the inlet velocity after the flow has traveled around 10% of the pipe length. The

other microchannels also reach the fully developed condition at the same location. However, the central velocity is higher for the triangular microchannel and lower for the rectangular microchannel compared to the circular microchannel. It is important to note that all microchannels have the same cross-sectional area, and the variation in velocity is solely due to the geometrical differences. In Figure 16(b), the temperature of the microchannel fluid is shown to decrease by approximately 21-24% for all microchannels. The circular microchannel exhibits a slightly higher temperature compared to the other microchannels due to its smaller surrounding surface area. Figure 16(c) displays the pressure profiles, indicating the highest pressure drop for the triangular microchannel and the lowest pressure drop for the circular microchannel, as expected.

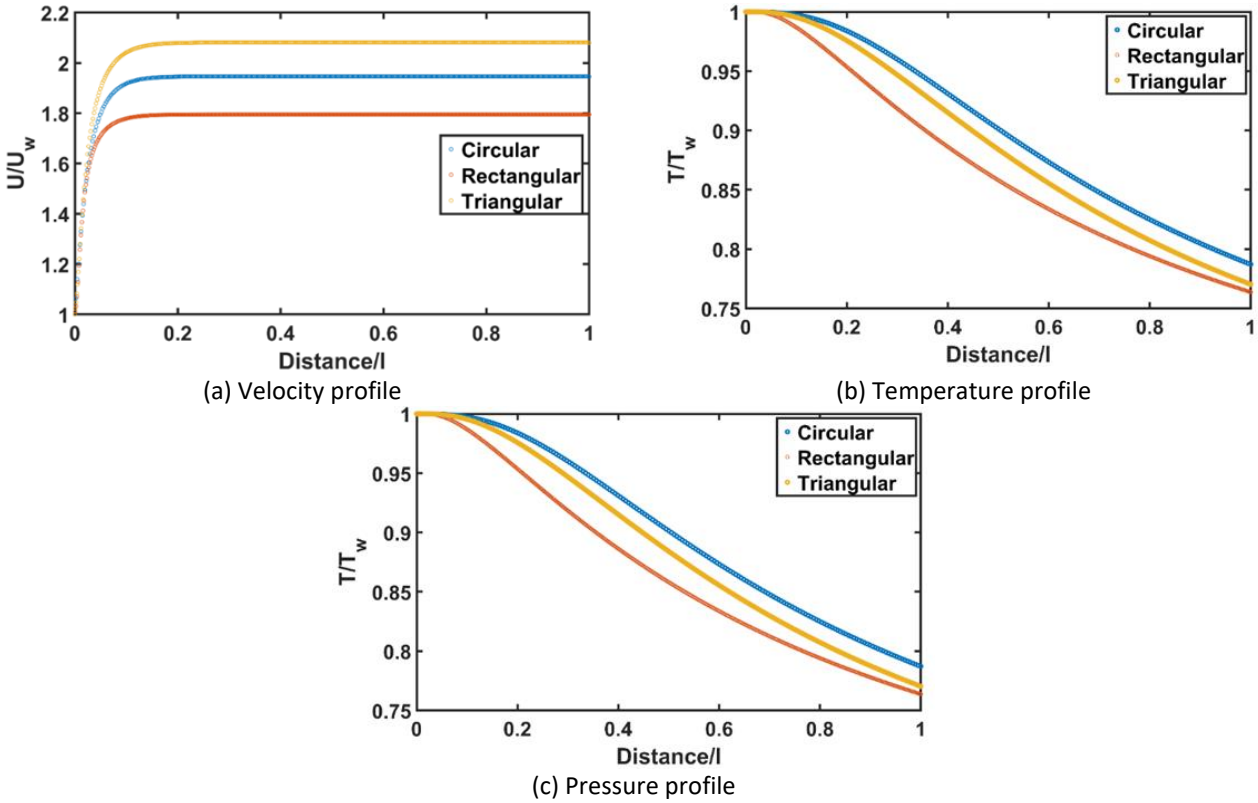

(a) Velocity profile (b) Temperature profile

(c) Pressure profile

Fig. 16. Velocity, temperature, and pressure distribution along centerline in the microchannel with different geometries

Figure 17 presents the radial velocity, temperature, and pressure profiles for the three microchannel geometries. The temperature and velocity profiles at the center of the midplane exhibit the highest values and gradually decrease as moving away from the center. However, the pressure profile remains constant, indicating a uniform pressure distribution at each section of the microchannel.

Among the considered geometries, the circular microchannel, which possesses the largest diameter, exhibits the lowest pressure drop. In a study conducted by Gunnasegaran *et al.,* [23], the influence of geometrical factors on the flow and heat transmission characteristics of the MCHE was investigated. Those results also revealed that the microchannel with the largest hydraulic diameter exhibited the lowest pressure drop.

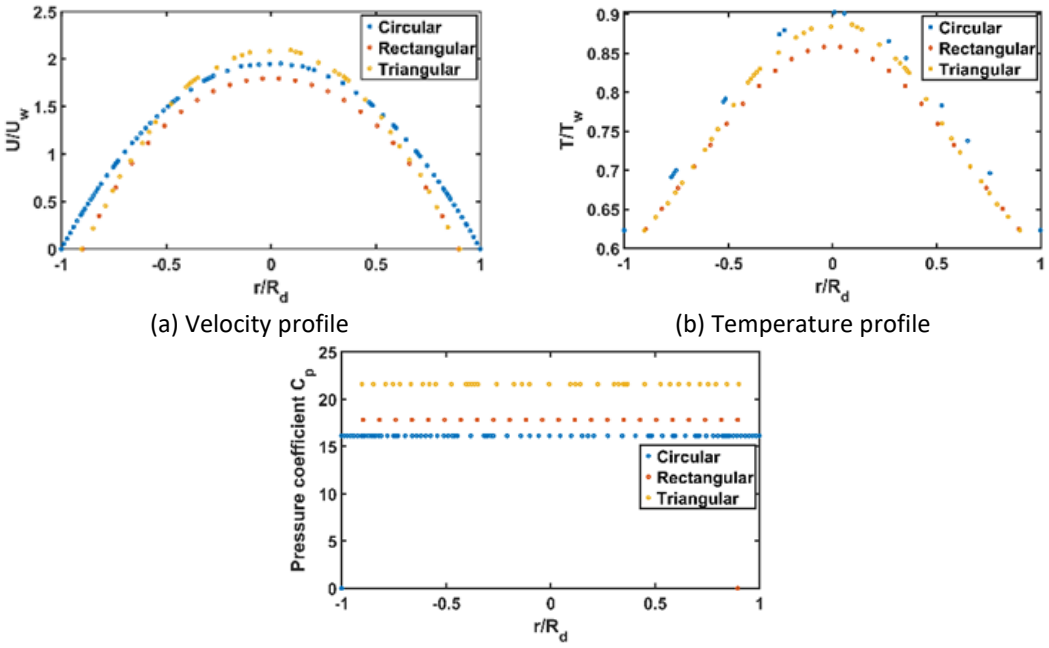

(a) Velocity profile (b) Temperature profile

(c) Pressure profile

Fig. 17. Radial distribution of velocity, temperature, and pressure in microchannels with different geometries

By analysing of the crossflow, solid domain, and microchannel, the effectiveness and performance index for all geometries were calculated. The effectiveness (ε) is calculated as

$$\varepsilon_{circular\ channel} = \frac{q}{q_{max}} = \frac{C_h(T_{w,in} - T_{w,out})}{C_{min}(T_{w,in} - T_{a,in})} \tag{5}$$

The performance index (η) is computed as

$$\eta = \frac{\varepsilon}{\Delta P} \tag{6}$$

The results are summarized in Table 4, which indicate that the rectangular microchannel exhibits the highest effectiveness among the tested geometries, while the circular microchannel has the lowest effectiveness. Conversely, the circular microchannel demonstrates the highest performance index value, indicating better overall efficiency, while the triangular microchannel has the lowest performance index value.

Table 4
Effectiveness and performance index of MCHE for different channel geometries

Microchannel Geometry	Effectiveness (ε)	Performance Index (η), ($\frac{m^2}{N}$)
Circular	0.467	6.91×10^{-4}
Triangular	0.497	5.79×10^{-4}
Rectangular	0.51	6.81×10^{-4}

4. Conclusions

In this study, high-fidelity conjugate heat transfer simulations are employed to investigate the thermal-hydraulic performance of an MCHE featuring louver-shaped fins in the presence of crossflow. The simulations tightly coupled the solid domain, microchannel flow, and crossflow field to accurately predict the temperature distribution within the solid and the flow variables in both the microchannel and crossflow regions. Three different MCHEs with circular, triangular, and square microchannel geometries were considered in the analysis. The local flow field investigations revealed significant variations in velocity and temperature within the crossflow. The temperature distribution within the solid domain exhibited non-uniformity in the spanwise direction due to changes in the temperature of the hot flow within the microchannel. However, the temperature remained relatively uniform within each section of the solid domain due to the high conductivity of aluminum. The results demonstrated that the circular MCHE exhibited the best performance, while the rectangular MCHE showed higher heat transfer effectiveness.

Acknowledgment
This research was not funded by any grant.

References

[1] Chen, C. S., and W. J. Kuo. "Heat transfer characteristics of gaseous flow in long mini-and microtubes." *Numerical Heat Transfer, Part A: Applications* 46, no. 5 (2004): 497-514. https://doi.org/10.1080/10407780490463773

[2] Yeo, Ilhwan, and Seunghyun Lee. "2D computational investigation into transport phenomena of subcooled and saturated flow boiling in large length to diameter ratio micro-channel heat sinks." *International Journal of Heat and Mass Transfer* 183 (2022): 122128. https://doi.org/10.1016/j.ijheatmasstransfer.2021.122128

[3] Park, Kyoungwoo, Kwan-Joong Noh, and Kwan-Soo Lee. "Transport phenomena in the thin-film region of a micro-channel." *International Journal of Heat and Mass Transfer* 46, no. 13 (2003): 2381-2388. https://doi.org/10.1016/S0017-9310(02)00541-0

[4] Sun, Hongwei, and Mohammad Faghri. "Effect of surface roughness on nitrogen flow in a microchannel using the direct simulation Monte Carlo method." *Numerical Heat Transfer: Part A: Applications* 43, no. 1 (2003): 1-8. https://doi.org/10.1080/10407780307302

[5] Beskok, Ali. "Validation of a new velocity-slip model for separated gas microflows." *Numerical Heat Transfer, Part B: Fundamentals* 40, no. 6 (2001): 451-471. https://doi.org/10.1080/104077901753306593

[6] Suman, Balram. "A steady state model and maximum heat transport capacity of an electrohydrodynamically augmented micro-grooved heat pipe." *International Journal of Heat and Mass Transfer* 49, no. 21-22 (2006): 3957-3967. https://doi.org/10.1016/j.ijheatmasstransfer.2006.04.011

[7] Yang, Chien-Yuh. "Friction characteristics of water, R-134a, and air in small tubes." *Microscale Thermophysical Engineering* 7, no. 4 (2003): 335-348. https://doi.org/10.1080/10893950390243608

[8] Wu, W., H. Bostanci, L. C. Chow, Y. Hong, C. M. Wang, M. Su, and John P. Kizito. "Heat transfer enhancement of PAO in microchannel heat exchanger using nano-encapsulated phase change indium particles." *International Journal of Heat and Mass Transfer* 58, no. 1-2 (2013): 348-355. https://doi.org/10.1016/j.ijheatmasstransfer.2012.11.032

[9] Chen, Yongping, Chengbin Zhang, Mingheng Shi, Jiafeng Wu, and G. P. Peterson. "Study on flow and heat transfer characteristics of heat pipe with axial "Ω"-shaped microgrooves." *International Journal of Heat and Mass Transfer* 52, no. 3-4 (2009): 636-643. https://doi.org/10.1016/j.ijheatmasstransfer.2008.08.003

[10] Fedorov, Andrei G., and Raymond Viskanta. "Three-dimensional conjugate heat transfer in the microchannel heat sink for electronic packaging." *International Journal of Heat and Mass Transfer* 43, no. 3 (2000): 399-415. https://doi.org/10.1016/S0017-9310(99)00151-9

[11] Kandlikar, Satish G., and William J. Grande. "Evaluation of single phase flow in microchannels for high heat flux chip cooling—thermohydraulic performance enhancement and fabrication technology." *Heat transfer engineering* 25, no. 8 (2004): 5-16. https://doi.org/10.1080/01457630490519772

[12] Dang, Thanhtrung, and Jyh-tong Teng. "Comparisons of the heat transfer and pressure drop of the microchannel and minichannel heat exchangers." *Heat and mass transfer* 47 (2011): 1311-1322. 10.1007/s00231-011-0793-9

[13] Herman, Cila, and Eric Kang. "Heat transfer enhancement in a grooved channel with curved vanes." *International Journal of Heat and Mass Transfer* 45, no. 18 (2002): 3741-3757. https://doi.org/10.1016/S0017-9310(02)00092-3
[14] Pan, Minqiang, Hongqing Wang, Yujian Zhong, Minglong Hu, Xiaoyu Zhou, Guanping Dong, and Pingnan Huang. "Experimental investigation of the heat transfer performance of microchannel heat exchangers with fan-shaped cavities." *International Journal of Heat and Mass Transfer* 134 (2019): 1199-1208. https://doi.org/10.1016/j.ijheatmasstransfer.2019.01.140
[15] Jiang, Pei-Xue, Ming-Hong Fan, Guang-Shu Si, and Ze-Pei Ren. "Thermal–hydraulic performance of small scale micro-channel and porous-media heat-exchangers." *International Journal of Heat and Mass Transfer* 44, no. 5 (2001): 1039-1051. https://doi.org/10.1016/S0017-9310(00)00169-1
[16] Brandner, J. J., E. Anurjew, L. Bohn, E. Hansjosten, T. Henning, U. Schygulla, A. Wenka, and K. Schubert. "Concepts and realization of microstructure heat exchangers for enhanced heat transfer." *Experimental Thermal and Fluid Science* 30, no. 8 (2006): 801-809. https://doi.org/10.1016/j.expthermflusci.2006.03.009
[17] Hasan, Mushtaq I., Abdul A. Rageb, M. Yaghoubi, and Homayon Homayoni. "Influence of channel geometry on the performance of a counter flow microchannel heat exchanger." *International Journal of Thermal Sciences* 48, no. 8 (2009): 1607-1618. https://doi.org/10.1016/j.ijthermalsci.2009.01.004
[18] Sui, Y., C. J. Teo, Poh Seng Lee, Y. T. Chew, and C. Shu. "Fluid flow and heat transfer in wavy microchannels." *International Journal of Heat and Mass Transfer* 53, no. 13-14 (2010): 2760-2772. https://doi.org/10.1016/j.ijheatmasstransfer.2010.02.022
[19] Al-Bakhit, Hussien, and Ahmad Fakheri. "Numerical simulation of heat transfer in simultaneously developing flows in parallel rectangular ducts." *Applied thermal engineering* 26, no. 5-6 (2006): 596-603. https://doi.org/10.1016/j.applthermaleng.2005.07.002
[20] Glazar, Vladimir, Anica Trp, and Kristian Lenic. "Optimization of air-water microchannel heat exchanger using response surface methodology." *International Journal of Heat and Mass Transfer* 157 (2020): 119887. https://doi.org/10.1016/j.ijheatmasstransfer.2020.119887
[21] Ahmed, Hossain, Seifollah Nasrazadani, and Hamid Sadat. "Comparison of Thermal Effectiveness and Crevice Corrosion Risk of Fin Geometry on All-Aluminum Microchannel Heat Exchangers." *Journal of Advanced Research in Fluid Mechanics and Thermal Sciences* 105, no. 2 (2023): 192-203.
[22] Deng, Yibin, Shyam Menon, Zoe Lavrich, Hailei Wang, and C. L. Hagen. "Design, simulation, and testing of a novel micro-channel heat exchanger for natural gas cooling in automotive applications." *Applied thermal engineering* 110 (2017): 327-334. https://doi.org/10.1016/j.applthermaleng.2016.08.193
[23] Gunnasegaran, Prem, H. A. Mohammed, N. H. Shuaib, and Rahman Saidur. "The effect of geometrical parameters on heat transfer characteristics of microchannels heat sink with different shapes." *International communications in heat and mass transfer* 37, no. 8 (2010): 1078-1086. https://doi.org/10.1016/j.icheatmasstransfer.2010.06.014